AD

AD-E403 948

Technical Report ARMET-TR-16085

U.S. ARMY ARMAMENT RESEARCH, DEVELOPMENT AND ENGINEERING CENTER GRAIN EVALUATION SOFTWARE TO NUMERICALLY PREDICT LINEAR BURN REGRESSION FOR SOLID PROPELLANT GRAIN GEOMETRIES

Brian Hunter
Carlton Adam
Adrian Blot
Pasquale Carlucci
Jonathan Jablonski

October 2017

U.S. ARMY ARMAMENT RESEARCH, DEVELOPMENT AND ENGINEERING CENTER

Munitions Engineering Technology Center

Picatinny Arsenal, New Jersey

The views, opinions, and/or findings contained in this report are those of the author(s) and should not be construed as an official Department of the Army position, policy, or decision, unless so designated by other documentation.

The citation in this report of the names of commercial firms or commercially available products or services does not constitute official endorsement by or approval of the U.S. Government.

Destroy by any means possible to prevent disclosure of contents or reconstruction of the document. Do not return to the originator.

REPORT DOCUMENTATION PAGE

Form Approved
OMB No. 0704-01-0188

1. REPORT DATE (DD-MM-YYYY)	2. REPORT TYPE	3. DATES COVERED (*From - To*)
October 2017	Final	August 2015 to September 2016

4. TITLE AND SUBTITLE

U.S. ARMY ARMAMENT RESEARCH, DEVELOPMENT AND ENGINEERING CENTER GRAIN EVALUATION SOFTWARE TO NUMERICALLY PREDICT LINEAR BURN REGRESSION FOR SOLID PROPELLANT GRAIN GEOMETRIES

5a. CONTRACT NUMBER

5b. GRANT NUMBER

5c. PROGRAM ELEMENT NUMBER

6. AUTHORS

Brian Hunter, Carlton Adam, Adrian Blot, Pasquale Carlucci, and Jonathan Jablonski

5d. PROJECT NUMBER

5e. TASK NUMBER

5f. WORK UNIT NUMBER

7. PERFORMING ORGANIZATION NAME(S) AND ADDRESS(ES)
U.S. Army ARDEC, METC
Fuze & Precision Armaments Technology Directorate
(RDAR-MEF-E)
Picatinny Arsenal, NJ 07806-5000

8. PERFORMING ORGANIZATION REPORT NUMBER

9. SPONSORING/MONITORING AGENCY NAME(S) AND ADDRESS(ES)
U.S. Army ARDEC, ESIC
Knowledge & Process Management (RDAR-EIK)
Picatinny Arsenal, NJ 07806-5000

10. SPONSOR/MONITOR'S ACRONYM(S)

11. SPONSOR/MONITOR'S REPORT NUMBER(S)
Technical Report ARMET-TR-16085

12. DISTRIBUTION/AVAILABILITY STATEMENT
Approved for public release; distribution is unlimited.

13. SUPPLEMENTARY NOTES

14. ABSTRACT

The ability to manufacture complex propellant grains with additive manufacturing processes necessitates the ability to numerically predict grain regression during the design process. A numerical tool developed by the U.S. Army Armament Research, Development and Engineering Center, Picatinny Arsenal, NJ, which uses an Eulerian volume-of-fluid approach to solve the phase-field equation, is able to accurately predict grain regression for arbitrary solid propellant geometries. Numerical results generated using this tool are validated against commonly-used propellant grain geometries with exact regression solutions, and the capability of the tool to analyze an additive-manufactured grain with complex internal structures is presented.

15. SUBJECT TERMS
Additive manufacturing Propellant grain Grain regression Progressivity Numerical analysis ABAQUS Volume of fluid Phase-field interface tracking

16. SECURITY CLASSIFICATION OF:			17. LIMITATION OF ABSTRACT	18. NUMBER OF PAGES	19a. NAME OF RESPONSIBLE PERSON
a. REPORT	b. ABSTRACT	c. THIS PAGE			Brian Hunter
U	U	U	SAR	25	19b. TELEPHONE NUMBER (Include area code) (973) 724-1461

Standard Form 298 (Rev. 8/98)
Prescribed by ANSI Std. Z39.18

CONTENTS

FIGURES

FIGURES
(continued)

ACKNOWLEDGMENTS

The authors would like to express their gratitude to the U.S. Army Armament Research, Development and Engineering Center, Picatinny Arsenal, NJ, Additive Manufacturing for Propulsion Technology program for funding this effort.

INTRODUCTION

Most cartridge-based munitions use some form of granular solid propellant (fig. 1), in which the deflagration process is modeled as a regression of grain surfaces along their respective surface normal (Piobert's Law of Burning, 1839). The propellant gas generation rate is well known to be dependent on both local pressure and the granular surface area. Control over the shape of solid propellant grain allows for a high degree of control over the propellant burn rate, burn time, and amount of generated propellant gases that directly impact the thrust versus time profile of the given system (ref. 1). Generally, grains with high progressivity, or grains whose burning surface area increase as the grain is consumed, are desired so that the generation rate of propellant gases increases during the munition launch cycle. Some typical approaches to increase propellant grain surface area are the addition of slotted/perforated features to the grain geometry (fig. 2).

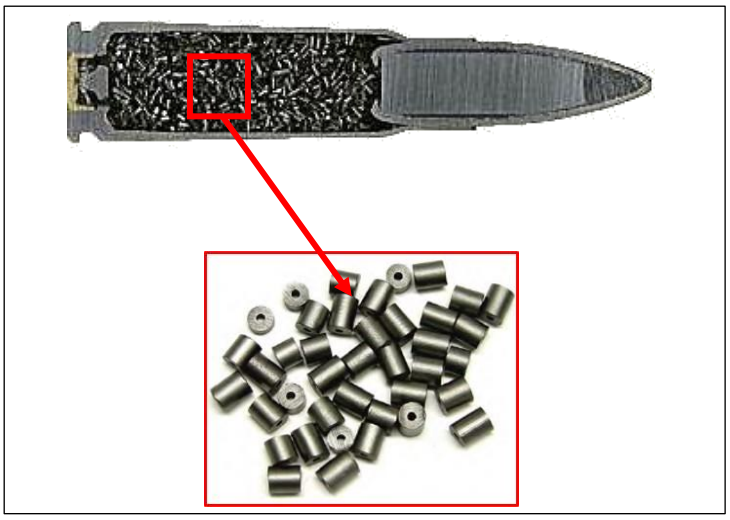

Figure 1
Cartridge-based munition containing single-perforation cylindrical propellant grains

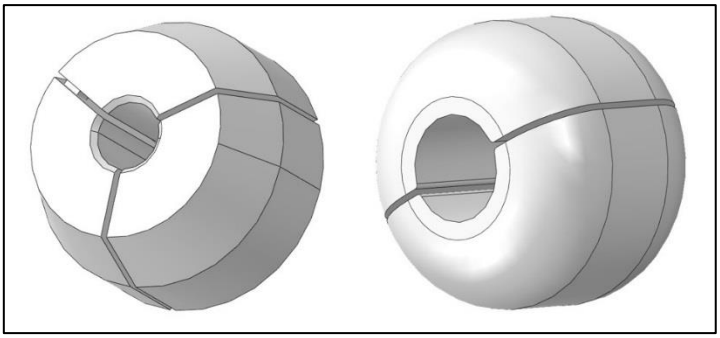

(a) M549 aft rocket motor (b) XM1128 rocket motor

Figure 2
Rocket motor geometries with slotted/perforated features to increase burn surface area

A common mathematical model that relates grain linear surface regression rate dx/dt to current local pressure $P_l(t)$ is Vieille's Law of 1893, shown in equation 1

$$\frac{dx}{dt} = AP_l^n(t) \tag{1}$$

where x equals $x(t)$ is the linear surface regression at time t, and A and n are constants that depend on the propellant composition. For simple propellant grain geometries, such as the single-perforation [perforation (cylinder with concentric hole)] grain, mathematical expressions for the unburnt grain mass $m_g(t)$ and gas generation rate dm_g/dt at a given time t can be readily determined from the initial grain geometry as shown in figure 3. In all forthcoming sections, the instantaneous linear surface regression $x(t)$ has been written as x for convenience.

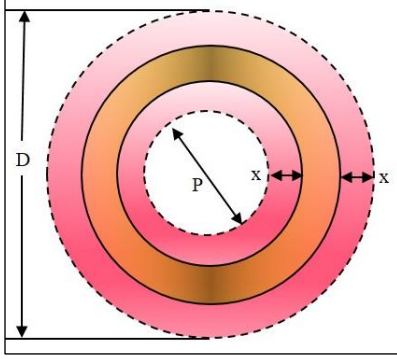

$$m_g(t) = \rho_g * V_g(t) = \rho_g \frac{\pi}{4}[(D - 2 * x)^2 - (P + 2 * x)^2](L - 2 * x)$$

$$\frac{dm_g(t)}{dx} = -\rho_g \frac{\pi}{2}(D + P)(D - P + 2L - 8 * x)$$

$$\frac{dm_g(t)}{dt} = \frac{dm_g(t)}{dx} * \frac{dx}{dt} = -AP_l^n(t)\rho_g \frac{\pi}{2}(D + P)(D - P + 2L - 8 * x)$$

Figure 3
Surface regression diagram and burn equations for single-perforation grain with initial outer diameter D, inner diameter P, and length L [not shown (ref. 2)]

The advent of additive manufacturing brings forth a new advantage in solid propellant technology – the ability to create grains of arbitrary shape with complex internal structures that allow for fine-tuning of the burning surface area over time, and thus, greater control of propellant burn rate. A consequence of these complex, additive geometries, however, is that analytical expressions and prediction of burn rates from surface regression can become infeasible or impossible to obtain. In order to facilitate additive propellant grain design optimization without requiring physical printing and costly burn testing, a numerical tool predicting temporal burn regression/rate curves from initial computer aided design (CAD) geometries is required.

To this end, the U.S. Army Armament Research, Development and Engineering Center (ARDEC), Picatinny Arsenal, NJ, developed the ARDEC grain evaluation software (AGES), a numerical tool to calculate burn regression and burn rate curves for arbitrary solid propellant geometry through use of phase-field interface tracking of the burning grain surface. The AGES uses a Eulerian volume of fluid approach to "track" the exterior surface of the grain over time. The numerical approach and development of AGES is outlined in this report, and numerical results are compared to analytical expressions for common propellant grain geometries as validation. Finally, AGES is applied to prototypical additively-manufactured grain geometry with complex internal geometries to showcase the effectiveness of this numerical approach.

PHASE-FIELD EQUATION

Numerical tracking of interfaces using an Eulerian (fixed-grid) method is commonly implemented in situations where explicit tracking of exact interface locations/coordinates are mathematically difficult (ref. 3). Examples of applications involve multiphase flows, co-extrusion, and phase-change problems. The general phase-field method for sharp interface tracking is implemented in AGES. Using this method, moving interfaces are tracked via the solution of the general phase-field interface advection equation

$$\frac{\partial \phi}{\partial t} + \boldsymbol{u} \cdot \nabla \phi = 0 \tag{2}$$

where ϕ is the phase-field and $\boldsymbol{u}$ is the interfacial velocity. Various kernel functions can be used to describe the variation of the phase-field ϕ normal to the interface. A common kernel function for ϕ is given by equation 3 (ref. 4)

$$\phi = -\tanh\left(\frac{n}{\sqrt{2}W}\right) = -\tanh\left(\frac{x'}{\sqrt{2}}\right) \tag{3}$$

where x' is the ratio between the normal distance of a point in the phase-field from the interface n and the width of the hyperbolic tangent profile W. The variation of ϕ with x' is shown in figure 4 for the hyperbolic tangent kernel. As the distance from the interface reaches a critical value, the phase-field value approaches a constant – a distinct advantage from the level-set method where the signed distance always increases. At the interface, the value of ϕ is exactly 0, while at locations sufficiently far away from the interface, $|\phi|$ $equals$ 1.

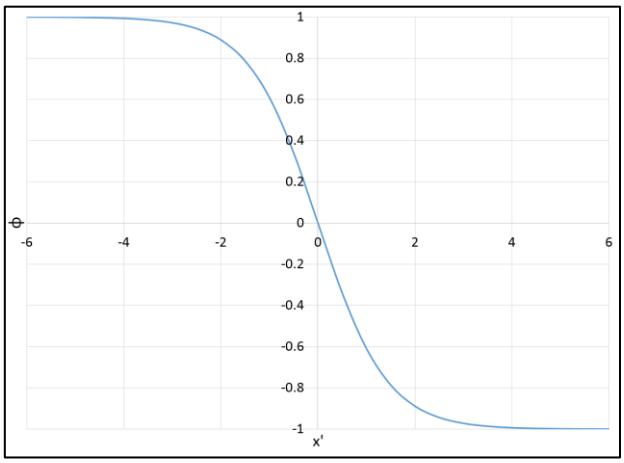

Figure 4
Variation of phase-field value ϕ around interface (x' equals 0)

For an interface that has no curvature-driven motion, equation 2 becomes

$$\frac{\partial \phi}{\partial t} + a|\nabla \phi| = b\left[\nabla^2 \phi + \frac{\phi(1-\phi^2)}{W^2} - |\nabla \phi| \nabla \cdot \left(\frac{\nabla \phi}{|\nabla \phi|}\right)\right] \tag{4}$$

where a is the interface velocity and b is a purely numerical parameter that controls the relaxation and smoothing of the interface. The terms on the left-hand side represent temporal and spatial changes in phase-field values, respectively. The first two terms on the right-hand side represent

interface curvature, and the third term is a curvature counter term that mathematically cancels the interface curvature terms at the leading order, while maintaining the hyperbolic tangent profile at the interface (ref. 5). For a more detailed derivation and explanation of the governing equation, see reference 4.

NUMERICAL DISCRETIZATION

Numerical implementation of equation 4 can be achieved using finite-differencing. Equation 4 is discretized on a three-dimensional rectangular grid with equal spacing in all three ordinate directions (i.e., $\Delta x \; equals \; \Delta y \; equals \; \Delta z$). This is critical for discretization of the Laplacian term $\nabla^2\phi$, which can be discretized using the highly-stable 19-point stencil (ref. 6)

$$\begin{aligned}\nabla^2\phi_{000} \cong [2(&\phi_{+00}+\phi_{-00}+\phi_{0+0}+\phi_{0-0}+\phi_{00+}+\phi_{00-}) \\ &+(\phi_{++0}+\phi_{-+0}+\phi_{+-0}+\phi_{--0}+\phi_{+0+}+\phi_{+0-}+\phi_{-0+}+\phi_{-0-}+\phi_{0++}+\phi_{0+-} \\ &+\phi_{0-+}+\phi_{0--})-24\phi_{000}]/\,(6\Delta x^2)\end{aligned} \tag{5}$$

where the notation ϕ_{+0-} indicates $\phi_{i+1,j,k-1}$ in traditional finite-differencing notation. Although the choice was made to implement a higher-order approximation to the Laplacian, the standard 7-point stencil for the Laplacian can be implemented without significant error for most cases. The gradient $\nabla\phi$ is discretized, using central differencing.

$$\nabla\phi_{000} \cong \frac{1}{2\Delta x}\left[\sqrt{(\phi_{+00}-\phi_{-00})^2+(\phi_{0+0}-\phi_{0-0})^2+(\phi_{00+}-\phi_{00-})^2}\right] \tag{6}$$

Finally, the curvature term is discretized in the following manner

$$|\nabla\phi_{000}|\nabla\cdot\left(\frac{\nabla\phi_{000}}{|\nabla\phi_{000}|}\right) \cong \frac{1}{\Delta x}\left[\phi_{Cx+}-\phi_{Cx-}+\phi_{Cy+}-\phi_{Cy-}+\phi_{Cz+}-\phi_{Cz-}\right] \tag{7}$$

where ϕ_{Cx+} and ϕ_{Cx-} can be expressed as

$$\begin{aligned}&\phi_{Cx+} \\ &= \frac{\phi_{+00}-\phi_{000}}{\sqrt{(\phi_{+00}-\phi_{000})^2+\frac{1}{16}(\phi_{++0}+\phi_{0+0}-\phi_{+-0}-\phi_{0-0})^2+\frac{1}{16}(\phi_{+0+}+\phi_{00+}-\phi_{+0-}-\phi_{00-})^2}} \\ &\phi_{Cx-} \\ &= \frac{\phi_{000}-\phi_{-00}}{\sqrt{(\phi_{000}-\phi_{00-})^2+\frac{1}{16}(\phi_{0+0}+\phi_{-+0}-\phi_{0-0}-\phi_{--0})^2+\frac{1}{16}(\phi_{00+}+\phi_{-0+}-\phi_{00-}-\phi_{-0-})^2}}\end{aligned} \tag{8}$$

and the remaining terms inside the square bracket can be expressed in a similar manner.

The temporal derivative in equation 4 is discretized using first-order forward-differencing with time step Δt. The numerical parameter W, corresponding to the width of the hyperbolic tangent profile in figure 4, must be defined small enough to resolve the ϕ profile numerically. To avoid overlapping of ϕ profiles for a curved interface, W should be kept as small as possible, although it is absolutely necessary that $W > \Delta x$. Parametric studies on W have shown that a value of $W \; equals \; 2\Delta x$ is suitable for most situations (ref. 4).

Finally, the numerical parameter b, which helps control problem stability and convergence, should adhere to the following relation

$$b < \frac{3\Delta x^2}{10\Delta t}(1 - 2Cr) \tag{9}$$

as described in reference 4, where the Courant number $Cr\ equals\ a\Delta t/\Delta x$. Typically, a value of $Cr\ equals\ 0.1$ provides sufficient accuracy without great increase in computational cost. The interface velocity a, in a sense, is therefore unimportant except to determine the necessary Δt to achieve the desired Cr for a given grid spacing. Therefore, for all simulations forthcoming, the interface velocity was set at a constant 0.5, and thus, the relationship between Δt and Δx becomes $\Delta t\ equals\ 0.05\Delta x$. Using this relation, equation 9 reduces to $b < 4.8\Delta x$.

PHASE-FIELD INITIALIZATION

Initialization of the numerical phase-field stems from the volume fraction of grain material that exists in each cell in the computational domain at $t\ equals\ 0$. Consider the two-dimensional (2D), five by five computational grid in figure 5a. For the circular grain shown (blue), the volume fraction of grain material existing in each computational cell is listed, ranging from 0.0 (no grain material exists in the cell) to 1.0 (the entire cell is comprised of grain material).

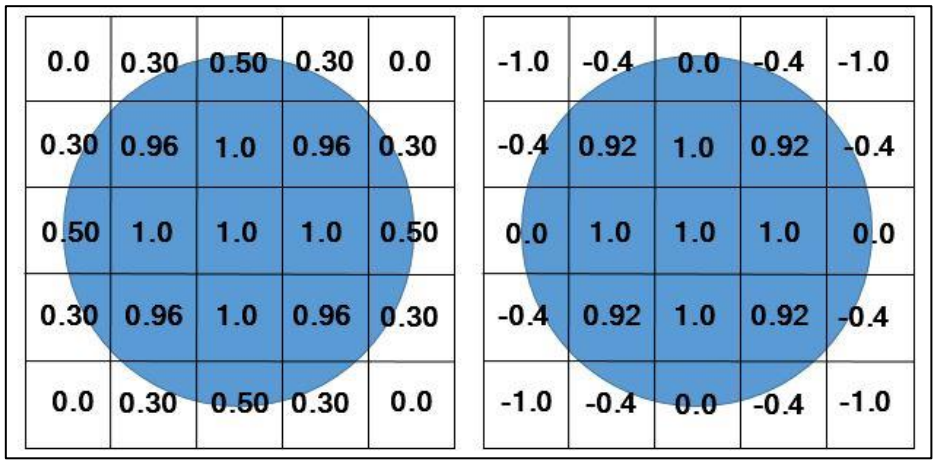

(a) Volume fraction in computational cells

(b) corresponding phase-field values

Figure 5
Phase-field initialization

To convert cell volume fraction to phase-field values, the following relationship is applied

$$\phi_{cell} = 2 * VF_{cell} - 1 \tag{10}$$

Using this relationship, a cell that is fully filled with grain material will have $\phi_{cell}\ equals\ 1.0$, and a cell that is fully void will have $\phi_{cell}\ equals\ -1.0$. These values echo the concept illustrated in figure 4, as cells that are either fully filled or fully empty do not intersect with the boundary interface. Phase-field values corresponding to the volume fractions of figure 5a are shown in figure 5b.

The linear relationship of equation 10 is further justified when considering the special case of $VF_{cell}\ equals\ 0.50$, where exactly half of the cell is filled with material. In the limit of zero boundary curvature (i.e., when Δx becomes sufficiently small), the boundary interface of the grain will pass directly through the cell center. As shown in figure 4, this situation corresponds to ϕ_{cell} equals 0.0, or zero signed distance between the cell center and the boundary interface. Substitution of $VF_{cell}\ equals\ 0.50$ into equation 10 produces the necessary $\phi_{cell}\ equals\ 0.0$.

U.S. ARMY ARMAMENT RESEARCH, DEVELOPMENT AND ENGINEERING CENTER GRAIN PREPROCESSING WITH ABAQUS/FINITE ELEMENT ANALYSIS (FEA)

In order to generate the phase-field inputs to AGES, the built-in volume fraction tool in ABAQUS/FEA, a commercial finite element package, is appropriated. Solid grain geometry can be imported into ABAQUS in a variety of different file formats. In conjunction with AGES, multiple Python scripts were developed to aid in the creation of the computational domain, which is generated using Eulerian elements. Once the propellant geometry is imported into ABAQUS, the user can set three variables: (1) the number of computational elements that will discretize the shortest side of the computational domain, (2) the domain extension past the minimum geometric bounds of the propellant grain, and (3) the accuracy of the volume fraction tool (low, medium, or high). Figure 6 shows a typical Eulerian computational domain generated in ABAQUS for a 7-perforation hex propellant grain. Once the computational Eulerian domain is generated, the built-in volume fraction tool can be run to get the fraction of each Eulerian cell that overlaps the solid geometry. This volume fraction is then converted into phase-field values using equation 10 and exported to a file for processing in the ARDEC grain evaluation software.

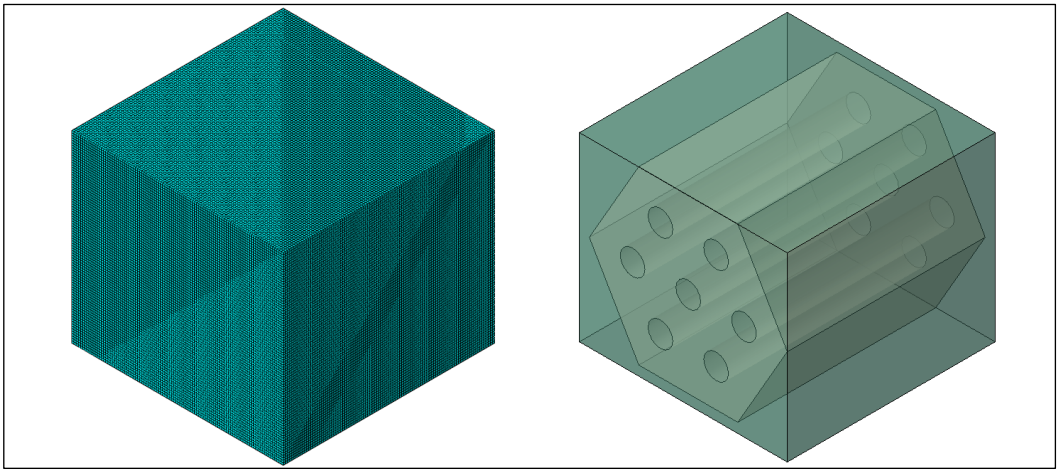

(a)
Eulerian domain with computational mesh visualized as generated in ABAQUS

(b)
Eulerian domain with propellant grain geometry fully enclosed

Figure 6
Typical Eulerian computational domain generated in ABAQUS for a 7-perforation hex propellant grain

RESULTS AND DISCUSSION

Validation, Spherical "Ball" Grain

As an initial validation case, consider a spherical "ball" grain of an initial unit diameter $(D_g\ equals\ 1.0)$. For spherical geometry, analytical expressions for the grain volume V_g and instantaneous change in grain volume dV_g/dx with respect to surface regression x can be written as

$$V_g(x) = \frac{\pi}{6}\left(D_g - 2x\right)^3$$
$$\frac{dV_g(x)}{dx} = -\pi\left(D_g - 2x\right)^2 \quad (11)$$

The quantity$-\ dV_g/dx$, which can be thought of as an instantaneous change in volume consumption, relates directly to the amount of propellant gas generated during the burn process.

Figure 7a compares results from AGES for grain volume V_g and change in volume consumption $-dV_g/dx$ versus burn distance x for the unit diameter spherical grain to the exact solutions of equation 11. The computational domain for this geometry was cubic in shape with a side length of 1.02 (in order to fully encapsulate the unit diameter sphere). The domain was discretized using either N equals 50, 100, or 200 elements per side, with the total number of elements in the domain equal to N^3. For this spherical geometry, total grain burnout should occur at x equals $D_g/2$ equals 0.50.

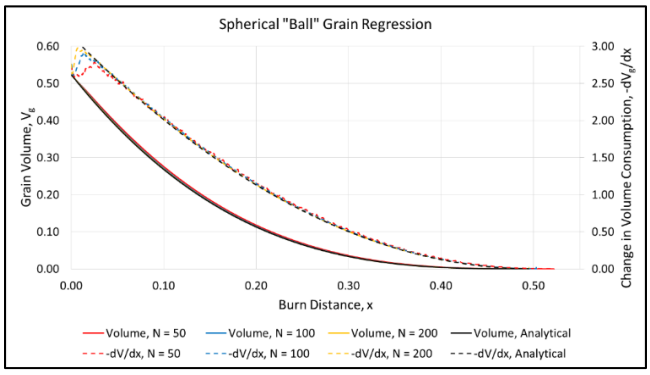

(a)
Grain volume and change in volume consumption

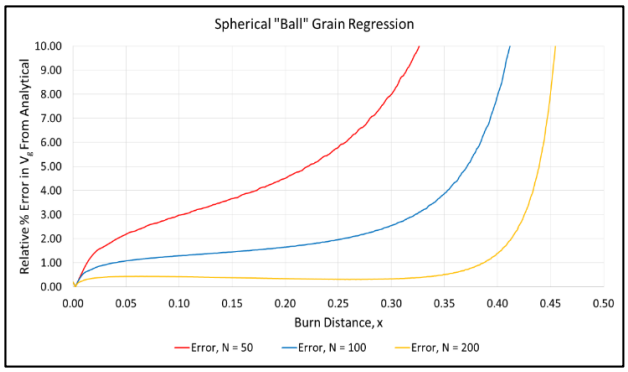

(b)
Relative percentage error in grain volume versus burn distance for spherical ball grain

Figure 7
Comparisons and results generated by AGES

Figure 7a shows that numerical results generated by AGES conform well to the analytical expressions in equation 11. Errors in $-dV_g/dx$ at initial small burn distances are witnessed due to the relaxation of the phase-field, as well as the faceted approximation of the smooth spherical ball surface with cubic elements. As seen in figure7b, the relative percentage error between the numerical and analytical approximations of grain volume V_g decrease with increasing element count. Errors are less than 1% for N equals 200 until x equals 0.387, at which point only ~1.2% of the initial grain volume remains unburnt. As the sphere volume becomes significantly small, the initial element discretization becomes unsuitable to properly capture grain regression, leading to larger errors. For N equals 200, errors of >10% occur at $x > 0.485$, at which point the percent of unburnt grain volume

is less than 0.1%. Total burnout for N equals 200 occurs at x equals 0.496, which is within 1% of the true value.

As previously discussed, the volume fraction tool in ABAQUS/FEA used to generate the initial phase-field has three accuracy methods: (1) low, (2) medium, and (3) high accuracy. Figure 8 shows a comparison of grain volume V_g and relative error in V_g versus burn distance x for the spherical grain for all three volume fraction tool accuracies using grid size of N equals 200. As expected, high accuracy produces the lowest overall errors as burn distance increases, although for a brief period after initial phase-field relaxation, medium accuracy produces more accurate solutions. The initial grain volume calculated using the three accuracies are 0.5178, 0.5196, and 0.5226, respectively. As compared to the true initial grain volume of 0.5236, it is clear that running the volume fraction tool at high accuracy is preferred to minimize numerical error.

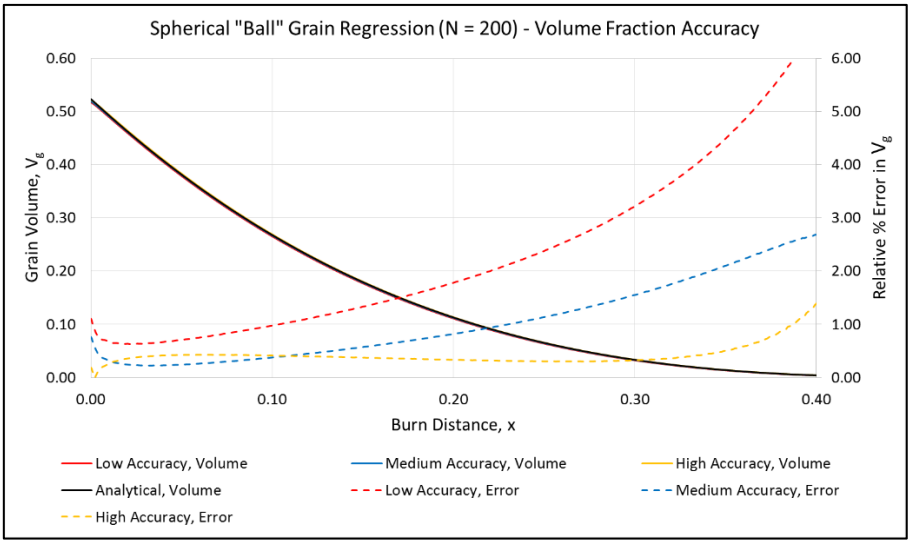

Figure 8
Grain volume and relative percentage error versus burn distance for spherical ball grain generated with low, medium, or high volume fraction accuracy

Single-Perforation Grain, Superposition Approach

A common propellant grain shape used in various munitions is the single-perforation, which is a cylindrical grain of diameter D_g and length L_g with a concentric hole of diameter P_g passing through the entire length. For such a grain, analytical expressions for V_g and dV_g/dx for a given burn distance x are easily calculated:

$$V_g(x) = \frac{\pi}{4}(L_g - 2x)\left[(D_g - 2x)^2 - (P_g + 2x)^2\right]$$
$$\frac{dV_g(x)}{dx} = -\frac{\pi}{2}\left[(D_g - 2x)^2 - (P_g + 2x)^2\right] + \frac{\pi}{4}(L_g - 2x)\left[-4(D_g - 2x) - 4(P_g + 2x)\right] \quad (12)$$

Figure 9 compares grain volume V_g and change in volume consumption -dV_g/dx versus burn distance x for a single-perforation propellant grain with initial D_g equals 1.0, L_g equals 2.0, and P_g equals 0.5. For such a grain, total burnout will occur at x equals 0.125. The computational domain has dimensions x equals 1.02, y equals 1.02, and z equals 2.04 to fully enclose the grain. Discretization of the domain is performed with three element densities: N_x $equals$ N_y $equals$ $0.5N_z$ $equals$ 101, 201, and 301. As seen for the spherical grain in figure 7a,

errors in $-dV_g/dx$ at small x occur due to initial phase-field relaxation and numerical faceting. After initial relaxation, numerical results conform well to the analytical expressions in equation 12 until burn distance becomes large. When 10% of the grain volume remains at x equals 0.075, the relative percentage errors in V_g are 26.1%, 8.87%, and 4.19% for the three element densities, respectively. Further grid refinement, while computationally expensive, would improve discrepancies between analytical and numerical results.

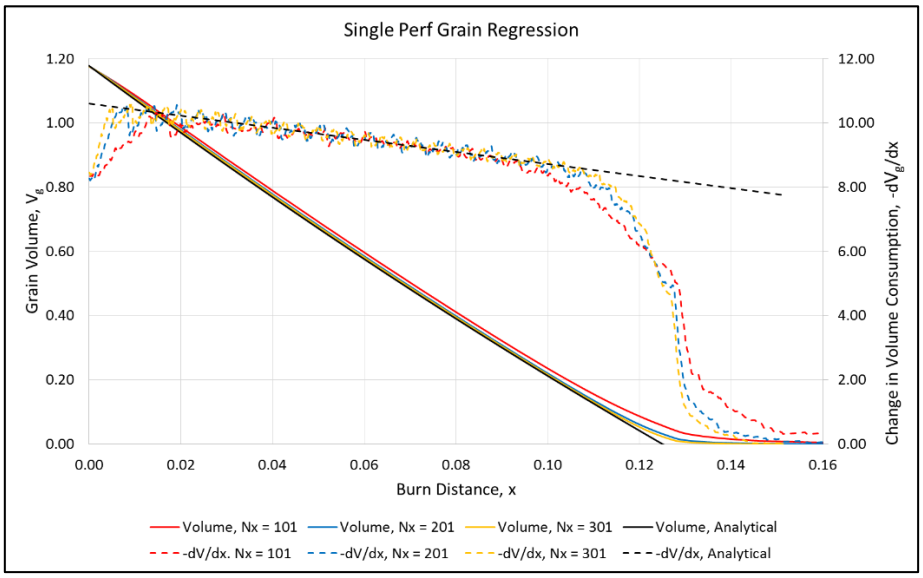

Figure 9
Grain volume and change in volume consumption versus burn distance for single-perforation grain

As the single-perforation grain approaches burnout, large numerical errors occur, which result in largely inaccurate burnout distances of 0.182, 0.162, and 0.151 for the three element densities, respectively. These large errors stem from the fact that, for the single-perforation grain, there are two interfaces that are being tracked: (1) the outer boundary of the grain, and (2) the interior perforated boundary. When these two interfaces approach one another during burn, significant diffusion between the two interfaces occurs. Additionally, the initial grid discretization becomes too small to accurately capture the volume in the small "sliver" of remaining grain geometry. Numerical errors due to interface diffusion will manifest much more greatly for grains with multiple interacting perforations, such as the common 7 or 19-perforation rod, and thus, a method to mitigate these types of errors is desired.

One method to mitigate interface diffusion errors is by applying a superposition technique. Consider the 2D approximation to the single-perforation grain in figure 10. Single-perforation grain regression can be effectively described as the superposition of two solid cylindrical grains: regression of a solid grain with diameter D_g minus the progression of a solid grain of diameter P_g. By treating a single-perforation grain as the superposition subtraction of two solid grains, the issue of multiple interface interaction/diffusion is entirely eliminated.

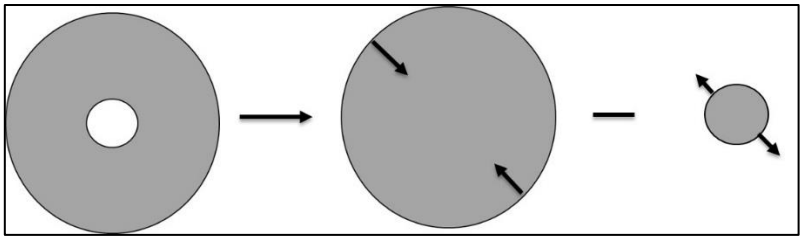

Figure 10
Illustration of superposition for 2D single-perforation grain

Using the superposition in figure 10, two phase-fields are initially generated: (1) ϕ_e, which captures the external boundary defined by D_g, and (2) ϕ_i, which captures the internal boundary defined by P_g. The internal phase-field ϕ_i is initialized in the opposite manner of ϕ_e (i.e., $\phi_{cell}\ equals -1$ inside the boundary, and $\phi_{cell}\ equals\ 1$ outside the boundary) so that the internal boundary will grow using the phase-field equation formulation. The volume of solid propellant in a single computational cell, therefore, can be calculated as:

$$V_{cell} = \Delta x \Delta y \Delta z [VF_e - VF_i] \tag{13}$$

where

$$\begin{aligned} VF_e &= \frac{1}{2}[\phi_e + 1] \\ VF_i &= \frac{1}{2}[1 - \phi_i] \end{aligned} \tag{14}$$

This methodology can be extended to grains with internal features or grains with multiple perforations that may interact with each other during grain regression.

In AGES, a scan over the elements in the computational domain is performed to determine the number of distinct internal features/cavities that exist in the grain geometry. These features can either be set to all burn immediately, or to burn only when a currently burning grain/feature boundary interacts with them for the first time. It should be mentioned that for each internal feature or cavity in the grain, the necessary computational memory resources will approximately double since a full phase-field for the full computational domain needs to be stored for each progressing/regressing feature.

For grains with fully enclosed internal features, it is straightforward to determine which computational cells encompass those features through a simple scanning algorithm. However, for grains with perforations through the entire grain (such as the single-perforation), it becomes more difficult to separate the features numerically. One method of ensuring that the perforation is fully captured so that superposition can be applied is to cap off the perforation CAD geometry with a thin layer of material, as shown in figure 11. The thickness of the cap layer should be greater than the side dimension of one computational element so that the geometry can be resolved. While this approach will add additional material to the grain (and thus, alter the initial volume V_g), by allowing the internal feature to burn immediately at the beginning of the analysis, the effects of the initial excess in volume become negligible as the burn distance, x, exceeds the cap thickness.

Figure 11
Cross section of single-perforation grain CAD geometry with capped perforation

A comparison of V_g and $-dV_g/dx$ versus x for a single-perforation grain, with numerical results generated with and without the superposition technique, to the exact solution is presented in figure 12 for N_x equals 301. A cap of thickness t_{cap} equals 0.0015 is added to the ends of the perforation for the superposition case, which is slightly larger than the element dimension $\Delta x\ equals$ 0.00134. Slight differences in V_g and dV_g/dx are witnessed at the onset of burning due to the additional cap material; however, the solutions become identical at x equals $\Delta x/2$, when the cap is completely burnt out. As x increases, the two solutions differ greatly due to the difference in interface treatment. When superposition is implemented, numerical results conform much more accurately to the analytical predictions. At x equals 0.12 (3.8% of initial grain remaining), the relative errors are 23.9% for the case without superposition and 7.3% for the case with superposition. When superposition is implemented, the predicted burnout distance decreases from 0.151 to 0.127, which is within 2% of the actual value of 0.125.

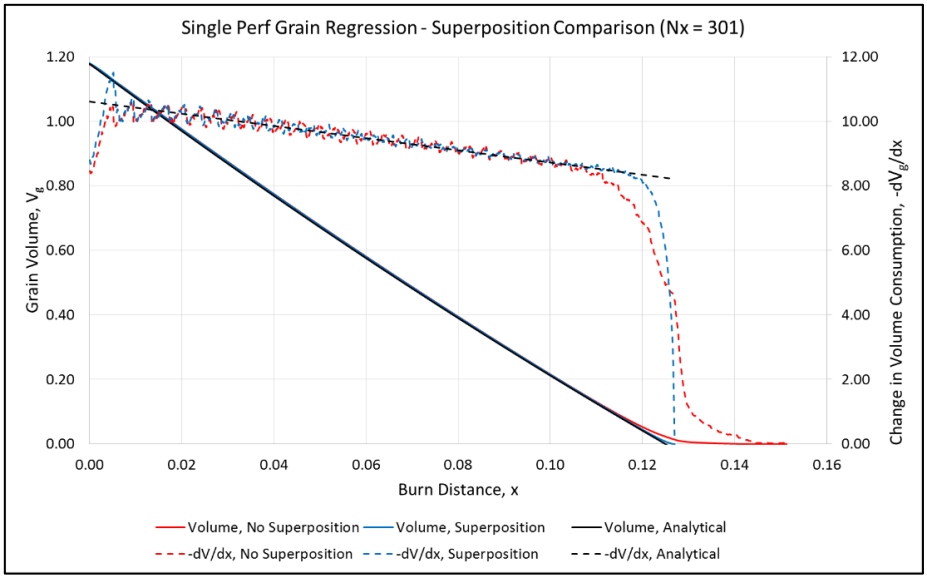

Figure 12
Grain volume and change in volume consumption for single-perforation propellant grain

Seven-Perforation Rod, Further Illustration of Superposition

To further illustrate the importance of using the superposition method, consider the 7-perforation cylindrical (rod) propellant grain of initial diameter D_g, length L_g, perforation diameter P_g, and web thickness w_g, as shown in figure 13. The web thickness w_g of a 7-perforation rod grain (or the distance between adjacent perforations or between perforations and outer diameter) is defined as $w_g\ equals\ D_g - 3P_g$. For this grain, expressions for V_g and dV_g/dx for a given burn distance $x \leq$

$w_g/2$ are a simple extension of equation 12, with a multiplier of seven added to $(P_g\ plus\ 2x)^2$ in the expression for V_g to account for the additional perforations. For $x > w_g/2$, however, the analytical expressions become more complex, as the intersections of the perforations both with the outer boundary and each other cause grain slivering (ref. 7), and thus, are not repeated here. The superposition method discussed in the previous section is best suited for predicting burn regression for this case, as it will be able to better capture the slivering behavior by avoiding diffused interfaces and small geometries.

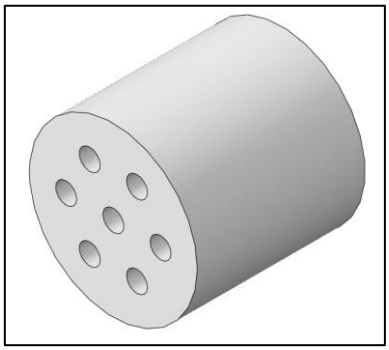

Figure 13
7-perforation rod grain geometry

Figure 14a plots a comparison of V_g and $-dV_g/dx$ profiles versus burn distance x for a 7-perforation rod grain with initial D_g equals 0.4, L_g equals 0.4, P_g equals 0.05, and w_g equals 0.0625 generated using AGES both with and without superposition to the analytical result. The numerical results are generated on a cubic domain of side length 0.404 using N equals 201 elements per side. For this grain, slivering begins at x equals 0.03125 and is indicated by the sharp decrease in dV_g/dx after the web has burnt out. Total burnout occurs at x equals 0.0512.

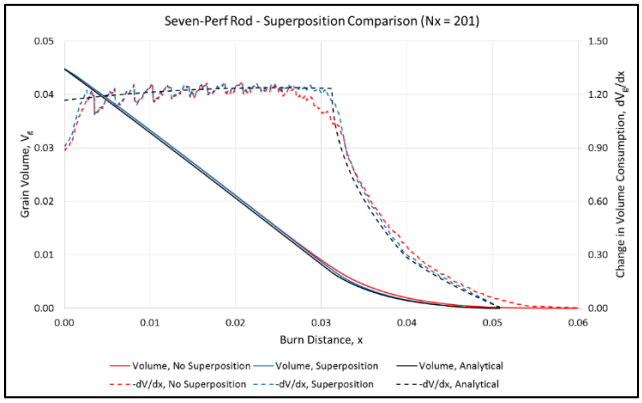

(a)

Grain volume and change in volume consumption

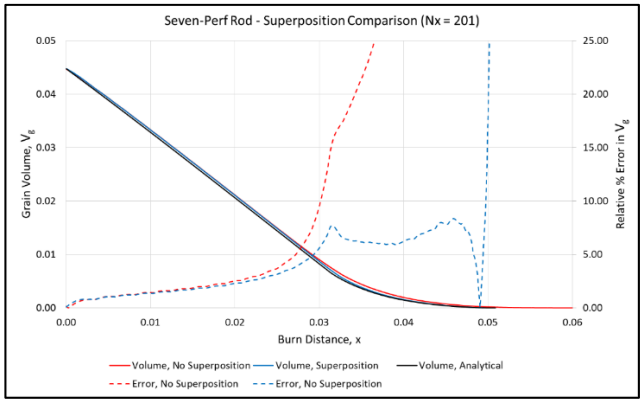

(b)

Relative percentage error in grain volume versus burn distance for 7-perforation rod propellant grain

Figure 14
7-perforation rod superposition comparisons

When superposition is ignored, significant errors in the numerical results occur well before slivering begins, and continue to dramatically increase throughout the burn duration. As seen in figure 14b, errors of over 15% are witnessed at the onset of slivering, and the total burnout distance over predicts the analytical by 27%. When superposition is included, and eight separate features (outer boundary and 7-perforations) are analyzed, greater agreement between numerical and analytical results is seen. Errors rise to ~7% at the onset of slivering but remain of similar magnitude until the grain has nearly burnt out at x equals 0.0509, which is within 1% of the analytical value.

Additive Manufacturing, "Fractal" Grain

As mentioned previously, an advantage of additive manufacturing is the ability to create complex grain geometries containing internal structures that become exposed after a certain portion of the initial grain burns away. Inclusion of complex internal structures and burn surfaces allow for greater control and fine-tuning of burn rate. A prototypical example of an additively-manufactured propellant grain geometry is shown in figure 15, which is referred to as a "fractal" grain. On the exterior (fig. 15a), this grain appears similar to a cylindrical rod grain. However, inside of the grain (fig. 15b and c), a large internal channel that spans the majority of the grain and branches out in multiple directions exists that will break the grain apart into pie-shaped fragments and dramatically increases the burning surface area. Additionally, as shown in figure 15d, 24 smaller internal subdivisions exist that will cause grain breakup at a later point in the ballistic cycle to further increase grain progressivity.

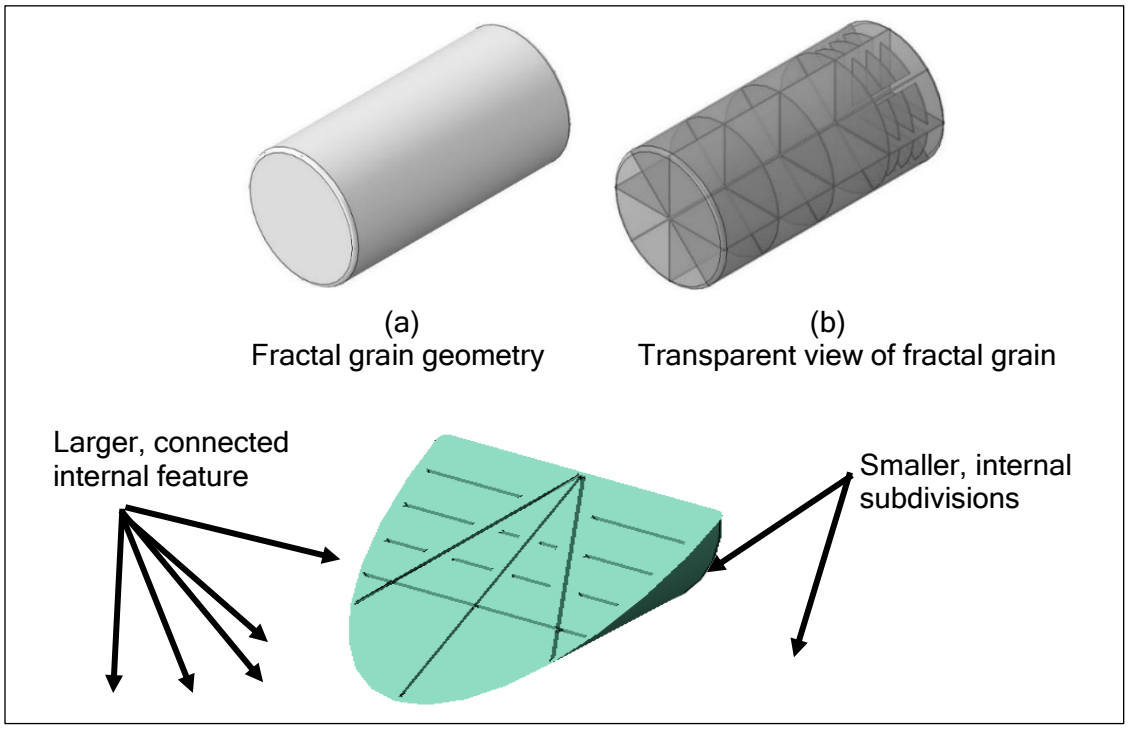

(a)
Fractal grain geometry

(b)
Transparent view of fractal grain

(c)
Angled cross section showing
larger connected internal feature

(d)
Angled cross-section showing
smaller internal subdivisions

Figure 15
A prototypical example of an additively-manufactured propellant grain geometry

In the previous section, non-physical caps were placed over perforations in order to apply superposition to be able to more accurately calculate grain regression characteristics. In order to

ensure that the addition of cap material to the perforations only had minimal impact, all of the internally detected features were allowed to burn as soon as the numerical analysis began. In a case such as this, all internal features should begin to burn when first intersected by another burning interface, whether that be an additional internal feature or regression of the outer grain boundary. The AGES allows for a user input to dictate whether internal features are allowed to burn immediately or based on intersection with another feature interface boundary. A representative output block from AGES for the aforementioned fractal grain is shown in figure 16, where callouts to the burn distance at which specific internal features begin to burn is explicitly stated.

```
-------------------------------------------
*******************************************
 OUTPUT BLOCK (FULL OUTPUT IN .SOLN FILE)
*******************************************
-------------------------------------------

Time at which Level Set Method Loop Begins =         1.668260989189E+02

 Distance_Burned        Burn_Fraction              dBF/dx      Unburnt_Volume               dV/dx
0.0000000000000E+00    0.0000000000000E+00   0.0000000000000E+00   1.4533662675068E+06   0.0000000000000E+00
Feature            1  is burning at burn distance  0.185661764705882
7.4264705882353E-01    1.1458646965077E+01   1.6064457917317E+01   1.2868301578036E+06  -2.3347541242808E+05
1.4852941176471E+00    2.3874876823010E+01   1.6411787348231E+01   1.1063768613523E+06  -2.3852338121412E+05
2.2279411764706E+00    3.5273649696391E+01   1.4898930868034E+01   9.4071094150090E+05  -2.1653603545517E+05
2.9705882352941E+00    4.5424357502194E+01   1.3087049976188E+01   7.9318397833820E+05  -1.9020276976566E+05
Feature            2  is burning at burn distance   3.08198529411765
Feature            3  is burning at burn distance   3.08198529411765
Feature            4  is burning at burn distance   3.08198529411765
Feature            5  is burning at burn distance   3.08198529411765
Feature            6  is burning at burn distance   3.08198529411765
Feature            7  is burning at burn distance   3.08198529411765
Feature            8  is burning at burn distance   3.08198529411765
Feature            9  is burning at burn distance   3.08198529411765
Feature           10  is burning at burn distance   3.08198529411765
Feature           11  is burning at burn distance   3.08198529411765
Feature           12  is burning at burn distance   3.08198529411765
Feature           13  is burning at burn distance   3.08198529411765
Feature           23  is burning at burn distance   3.08198529411765
Feature           25  is burning at burn distance   3.08198529411765
Feature           17  is burning at burn distance   3.08941176470588
Feature           19  is burning at burn distance   3.09683823529412
Feature           14  is burning at burn distance   3.11169117647059
Feature           16  is burning at burn distance   3.11169117647059
Feature           18  is burning at burn distance   3.11169117647059
Feature           15  is burning at burn distance   3.15625000000000
Feature           20  is burning at burn distance   3.15625000000000
Feature           21  is burning at burn distance   3.15625000000000
Feature           22  is burning at burn distance   3.15625000000000
Feature           24  is burning at burn distance   3.15625000000000
3.7132352941176E+00    5.5470325453437E+01   1.3137916274530E+01   6.4717926889029E+05  -1.9094204338729E+05
4.4558823529412E+00    6.4380086863421E+01   1.1481912916160E+01   5.1768780204225E+05  -1.6687424918796E+05
```

Figure 16
Output block from AGES for fractal grain with N equals 78 M cells

Figure 17 plots grain volume and change in volume consumption for the fractal grain shown in figure 15, generated with a total of 31, 78, and 128-million computational cells, respectively. For all three grid resolutions, the numerically calculated initial grain volume V_g is within 0.5% of the actual value with slight errors occurring due to curvature approximation using cubic elements. As the grain begins to burn, the largest internal feature starts to burn at an analytical burn distance of x equals 0.19228, which is the shortest linear distance between the surface of the feature and the outer boundary. For all three grid resolutions, the numerically calculated burn distances of x equals 0.17 to 0.18 are accurate to within the edge length of one computational cell, which is the maximum accuracy that can be achieved using the current method. The large increase in total burning surface area resulting from the ignition of the large internal feature causes a spike in dV_g/dx, showcasing the progressivity of the grain.

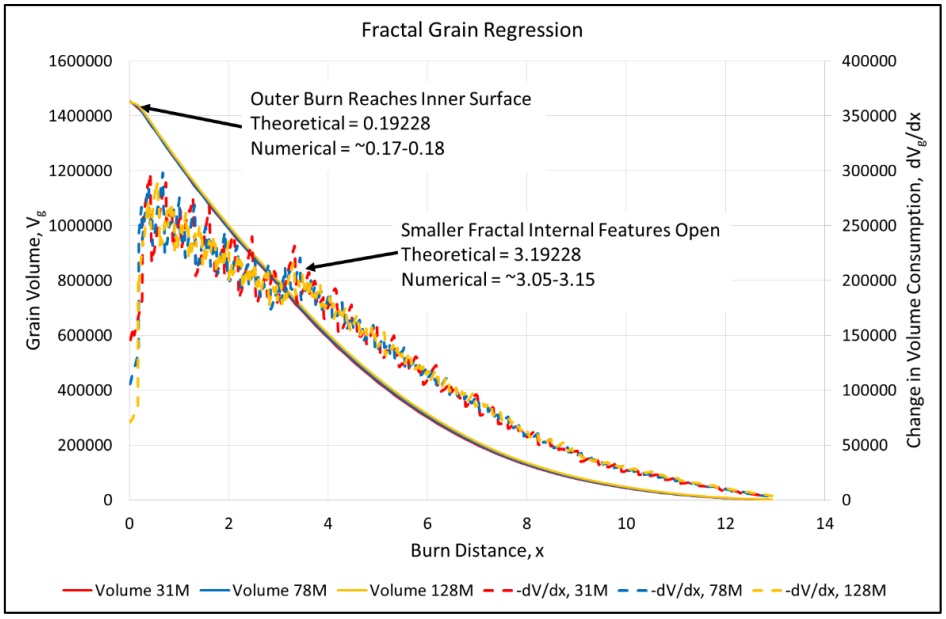

Figure 17
Grain volume and change in volume consumption for additively-manufactured fractal grain with total computational cell counts of 31, 78, and 128 million

As burning continues, a smaller spike in dV_g/dx is witnessed between x equals 3.05 to 3.15, resulting from the ignition of the 24 smaller internal features shown in figure 15d. These features begin to burn when intersected by the already burning large internal feature. The initial minimum distance between the larger internal feature and the 24 smaller features is x equals 3, and thus, analytically, the burn event for these smaller features should begin at x equals 3.19228. The numerically predicted burn distances where the internal features begin to burn are accurate and within 1 to 5%.

The agreement between the predicted burn distances and the theoretical values obtained from inspection of the CAD geometry showcase the ability of AGES to provide valuable information about the burn characteristics of arbitrarily-shaped, complex additive manufactured grains without requiring printing and testing of said geometries.

CONCLUSIONS

The ability to create complex, arbitrarily-shaped propellant grains with internal features using additive manufacturing processes allows for greater control over propellant gas generation during munition launch cycle. The U.S. Army Armament Research, Development and Engineering Center, Picatinny Arsenal, NJ, grain evaluation software (AGES) was developed to accurately predict propellant grain regression for arbitrary geometries using numerical methods, in order to allow for quick analysis of grain regression characteristics without requiring grain printing or costly burn testing. The AGES has been validated against commonly-used propellant grain geometries, and the capability of AGES to analyze complex geometries with intricate internal features is presented. The AGES is government owned, developed, and maintained.

REFERENCES

1. Carlucci, D.E. and Jacobson, S.S., “Ballistics: Theory and Design of Guns and Ammunition, 2nd Edition,” CRC Press, Boca Raton, FL, 2014.

2. Jablonski, J., Carlucci, P., Arata, J., and Ji, H., “Novel Approach in Coupling Interior Ballistic Models to Finite Element Codes,” 27th Army Science Conference Proceedings, Orlando, FL, November 2010.

3. Sethian, J.A., “Numerical Algorithms for Propagating Interfaces: Hamilton-Jacobi Equations and Conservation Laws,” Journal of Differential Geometry, Vol. 31, 1990.

4. Sun, Y. and Beckermann, C., “Sharp Interface Tracking Using the Phase-Field Equation,” Journal of Computational Physics, Vol. 220, pp. 626-653, 2007.

5. Folch, R., Casademunt, J., and Hernandez-Machado, A., “Phase File Model for Hele-Shaw Flows with Arbitrary Viscosity Contrast I Theoretical Approach,” Physical Review E, Vol. 60, p. 1724, 1999.

6. O'Reilly, R.C. and Beck, J.M., “A Family of Large-Stencil Discrete Laplacian Approximations in Three Dimensions,” International Journal for Numerical Methods in Engineering, pp. 1-16, 2006.

7. White, K.J., “Effect of Propellant Grain Dimensions on Progressivity,” Technical Report ARL-TR-1532, U.S. Army Research Laboratory, Adelphi, MD, 1997.

DISTRIBUTION LIST

U.S. Army ARDEC
ATTN: RDAR-EIK,
RDAR-MEE-P, C. Adam
RDAR-MEF-E, B. Hunter (2)
A. Blot
P. Carlucci
J. Jablonski
Picatinny Arsenal, NJ 07806-5000

Defense Technical Information Center (DTIC)
ATTN: Accessions Division
8725 John J. Kingman Road, Ste. 0944
Fort Belvoir, VA 22060-6218

GIDEP Operations Center
P.O. Box 8000
Corona, CA 91718-8000
gidep@gidep.org

REVIEW AND APPROVAL OF ARDEC TECHNICAL REPORTS

ARDEC GRAIN EVALUATION SOFTWARE TO NUMERICALLY PREDICT GRAIN RECESSION FOR ARBITRARY SOLID PROPELLANT GEOMETRIES
Title

Date received by LCSD

BRIAN HUNTER et. al
Author/Project Engineer

Report number (to be assigned by LCSD)

X1461 Extension

94 Building

RDAR-MEF-E
Author's/Project Engineers Office
(Division, Laboratory, Symbol)

PART 1. **Must be signed before the report can be edited.**

a. The draft copy of this report has been reviewed for technical accuracy and is approved for editing.

b. Use Distribution Statement A X, B____, C____, D____, E____, F____ or X____ for the reason checked on the continuation of this form. Reason: _____

1. If Statement A is selected, the report will be released to the National Technical Information Service (NTIS) for sale to the general public. Only unclassified reports whose distribution is not limited or controlled in any way are released to NTIS.

2. If Statement B, C, D, E, F, or X is selected, the report will be released to the Defense Technical Information Center (DTIC) which will limit distribution according to the conditions indicated in the statement.

c. The distribution list for this report has been reviewed for accuracy and completeness.

Robert Lee 8/29/2016
Division Chief (Date)

PART 2. To be signed either when draft report is submitted or after review of reproduction copy.

This report is approved for publication.

Robert Lee 8/29/2016
Division Chief (Date)

Andrew Pskowski 11/11/7
RDAR-CIS (Date)

LCSD 49 supersedes SMCAR Form 49, 20 Dec 06